Hotspot relaxation dynamics in a current-carrying superconductor

F. Marsili, M. J. Stevens, A. Kozorezov, V. B. Verma, Colin Lambert, J. A. Stern, R. D. Horansky, S. Dyer, S. Duff, D. P. Pappas, A. E. Lita, M. D. Shaw, R. P. Mirin, and S. W. Nam

Phys. Rev. B **93**, 094518 — Published 17 March 2016

DOI: 10.1103/PhysRevB.93.094518

Hotspot Relaxation Dynamics in a Current-Carrying Superconductor

F. Marsili[1*], M. J. Stevens[2], A. Kozorezov[3], V. B. Verma[2], Colin Lambert[3], J. A. Stern[1], R. Horansky[2], S. Dyer[2], S. Duff[2], D. P. Pappas[2], A. Lita[2], M. D. Shaw[1], R. P. Mirin[2], and S. W. Nam[2]

[1]*Jet Propulsion Laboratory, California Institute of Technology, 4800 Oak Grove Dr., Pasadena, California 91109, USA*

2National Institute of Standards and Technology, 325 Broadway, Boulder, CO 80305, USA

[3]*Department of Physics, Lancaster University, Lancaster, UK, LA1 4YB*

[*]*corresponding author: francesco.marsili.dr@jpl.nasa.gov*

We experimentally studied the dynamics of optically excited hotspots in current-carrying WSi superconducting nanowires as a function of bias current, bath temperature and excitation wavelength. We observed that the hotspot relaxation time depends on bias current, temperature, and wavelength. We explained this effect with a model based on quasi-particle recombination, which provides insight into the quasiparticle dynamics of superconductors.

I. INTRODUCTION

When a photon is absorbed in a superconductor, it creates a non-equilibrium region referred to as a *hotspot* [1]. The optical excitation of hotspots underpins the operation of most superconducting single photon detectors, such as microwave kinetic inductance detectors (MKIDs) [2, 3], superconducting tunnel junctions (STJs) [4], and superconducting nanowire single-photon detectors (SNSPDs) [5, 6]. The microscopic description of hotspot dynamics is a complicated, long-standing problem in non-equilibrium superconductivity [1]. If hotspot dynamics were better understood and controlled, many of the current limitations of these detectors could be overcome, potentially enabling disruptive technological advances.

Here we report a combined experimental and theoretical study of hotspots excited by single photons in a current-carrying WSi superconducting nanowire. We measured the hotspot relaxation dynamics in the nanowires as a function of bias current, bath temperature, and excitation wavelength. We observed that: (1) hotspot relaxation depends on the current carried by the nanowires; and (2) the current dependence of the relaxation time changes with bath temperature and excitation wavelength. The agreement between theory and experiment

provides insight into the quasiparticle dynamics of superconductors and the photodetection mechanism of superconducting single-photon detectors.

Hotspot formation is initiated when one photon is absorbed in a thin superconducting film, creating a non-equilibrium distribution of quasiparticles (QPs). The excited QPs down-convert from higher-energy states by exchanging energy with the electron and phonon systems. During the decay, further Cooper pairs are broken, increasing the number of QPs [1, 7]. Previously, the relaxation of optically excited superconductors was studied with optical and THz pump-probe techniques [8-10]. These techniques offer sub-ps time resolution, but are not sensitive enough to study the evolution of a single hotspot, and are difficult to perform below ~ 5 K. In this work, we used a different technique that combines the single-hotspot sensitivity of electrical readout with the high time resolution of ultrafast optical pump-probe spectroscopy [11, 12].

II. ONE- AND TWO-PHOTON DETECTION REGIMES

If an SNSPD produces a response pulse (or *click*) when a single photon creates a single hotspot, the detector operates in the *single-photon detection regime*, as shown in Figure 1 a. When the bias current is lowered to a point that a click can be efficiently triggered only if two photons generate two overlapping hotspots [5, 11, 13], the SNSPD operates in the *two-photon detection regime*, as shown in Figure 1 b. The current ranges in which the detector operates in single- or two-photon detection regimes depend on operating temperature and excitation wavelength.

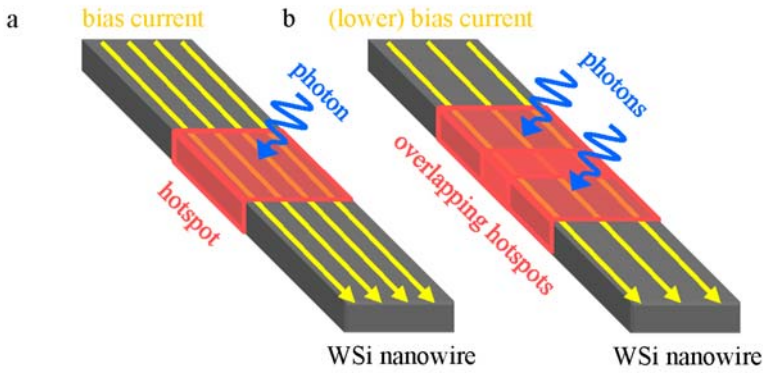

Figure 1. a. Representation of the single-photon detection regime. The current-biased superconducting nanowire produces a response pulse when a single photon creates a single hotspot (in red). **b.** Representation of the two-photon detection regime. The nanowire, biased at a lower current, produces a response pulse when two photons generate two overlapping hotspots.

To isolate the bias range for two-photon detection at a certain temperature and wavelength, we measured the single- and two-photon system detection efficiencies at a series of bias currents using the detector tomography method described in Ref. [14]. To determine the temperature and wavelength dependence of the single- and two-photon detection bias ranges, we measured the current dependence of the single-photon detection efficiency at different temperatures and wavelengths.

The detector studied was a fiber-coupled WSi SNSPD [15, 16] based on ~ 5 nm thick, 130 nm-wide nanowires spaced on a 200 nm pitch, meandering over an 11 μm-diameter circular active area. The SNSPD was operated in an adiabatic demagnetization refrigerator, in the temperature range T_B = 0.25 - 2 K.

A. Detector Tomography

The source of optical excitation was a fiber-based mode-locked laser with 1550 nm wavelength, ~ 5 ps pulse duration, and 36 MHz repetition rate (f_{rep}). As shown in Figure 2, we coupled the source through three fiber attenuators in series and then to a calibrated fiber switch. The switch had two output ports: one to a calibrated power meter and the other to the SNSPD detection system. To determine the mean number of photons per pulse incident on the SNSPD (μ), we calibrated the attenuators with the same procedure adopted in Ref. [16]. To calibrate an attenuator, we: (1) directed the switch output to the power meter, (2) measured the power with all three attenuators set to zero attenuation, and (3) measured the power with the attenuator under test set to the desired attenuation and the other two attenuators set to zero attenuation. This procedure was repeated for each attenuator for a range of nominal attenuations from zero to ~ 40 dB.

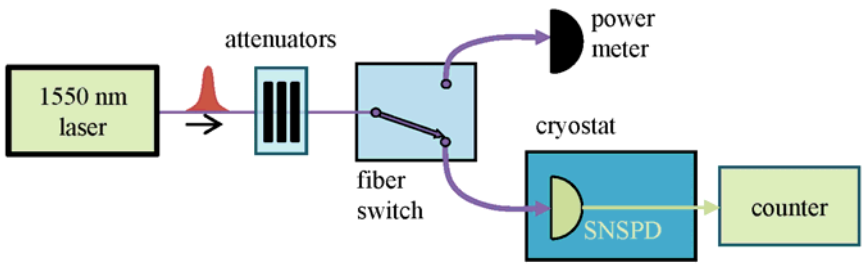

Figure 2. Experimental apparatus for the tomography measurements. The 1550 nm laser was a fiber-based mode-locked laser with ~ 5 ps pulse duration and f_{rep} = 36 MHz repetition rate.

Once the attenuators were calibrated, we turned on all three attenuators, directed the switch output to the SNSPD, and measured the probability of detection per optical pulse, which we called click probability $P_{\text{click}} = PCR / f_{\text{rep}}$. The photoresponse count rate, PCR, was estimated as the difference between the count rate (CR) measured from the SNSPD when the source was coupled to the device and the background count rate (BCR), measured with the source blocked. Figure 3 a shows the P_{click} vs μ curves measured for five values of I_B (colored squares).

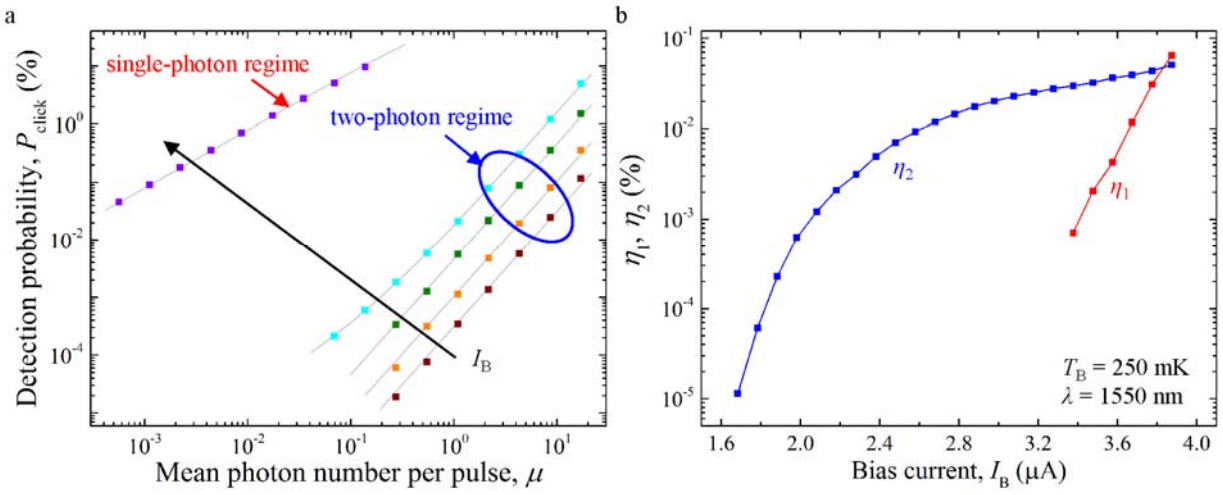

Figure 3. a. Detector click probability (P_{click}) vs mean photon number per pulse (μ) for several fixed values of the bias current I_B = 7.86 μA (violet), 3.48 μA (cyan), 2.58 μA (green), 2.18 μA (orange), 1.98 μA (dark red). The black arrow indicates the direction of increasing I_B. Solid gray curves are fits of the data to Equation (1). At 7.86 μA (blue curve), the SNSPD operates in the single-photon-detection regime. At the other four bias currents shown, the SNSPD operates in the two-photon-detection regime (although a weak one-photon component is visible at 3.48 μA). **b.** Fit values for single- and two-photon system detection efficiencies for a series of bias currents. The detector response is dominated by two-photon detection for bias currents $1.9\,\mu\text{A} \le I_B \le 3.5\,\mu\text{A}$, because $\eta_2 >> \eta_1$. These measurements were performed at λ = 1550 nm and T_B = 0.25 K.

In the limit where only one- and two-photon processes lead to a measurable count rate, P_{click} can be written as [14]:

$$P_{\text{click}}(\mu) = 1 - e^{-\mu} \sum_{n=0}^{\infty} \frac{\mu^n}{n!} (1-\eta_1)^n (1-\eta_2)^{n(n-1)/2} \qquad (1)$$

where η_1 and η_2 are the single- and two-photon system detection efficiencies. We defined η_1 as the probability that a photon coupled into the fiber connected to the SNSPD triggered a response pulse. Similarly, we defined η_2 as

the probability that two photons coupled into the fiber connected to the SNSPD triggered a response pulse. To be consistent with the background-subtracted data, Equation (1) ignores the effect of dark counts. In the single-photon detection regime, $\eta_1 >> \eta_2$ and Equation (1) simplifies to $P_{\text{click}}(\mu) = 1 - \exp(-\eta_1 \cdot \mu)$. If $\eta_1 \cdot \mu << 1$, we obtain the familiar approximation: $P_{\text{click}}(\mu) \sim \eta_1 \cdot \mu$. By contrast, if the detector operates in the two-photon detection regime (where $\eta_2 >> \eta_1$) and if $\eta_2 \cdot \mu^2 << 1$, then Equation (1) can be approximated by $P_{\text{click}}(\mu) \sim \eta_2 \cdot \mu^2 / 2$.

The solid gray curves in Figure 3 a are fits to the data using Equation (1) with η_1 and η_2 as fitting parameters [14]. At the highest bias current ($I_B = 7.86$ μA, blue squares), the device operated in the single-photon detection regime, with $\eta_1 \sim 80$ % and η_2 too small to be determined accurately. Because the single-photon detection efficiency of our device was higher than that of the device used in Ref. [14], it was not necessary to use the scaling procedure described in Ref. [14]. The data used for fitting were limited to those where $\mu \leq 20$ and $2.8 \times 10^{-6} \leq P_{\text{click}} \leq 0.1$. The sum in Equation (1) was truncated at a photon number of $N = 60$. Figure 3 b shows the bias dependence of the values of η_1 and η_2 that fit the experimental results. For $1.9\ \mu\text{A} \leq I_B \leq 3.5\ \mu\text{A}$, the SNSPD operated in the two-photon-detection regime, with $\eta_1 \ll \eta_2$.

B. Cutoff Current

To quantify how the bias ranges of the single- and two-photon detection regimes changed with bath temperature and excitation wavelength, we measured the temperature and wavelength dependence of the *PCR* vs I_B curves. To excite the detector with wavelengths other than 1550 nm, the pulsed laser source was sent through a highly nonlinear fiber to generate a supercontinuum spanning a wavelength range of 1200 - 1650 nm. We selected a given excitation wavelength with one of several bandpass filters placed between the supercontinuum source and the detector.

Figure 4 a shows *PCR* vs I_B curves at several bath temperatures from $T_B = 0.25$ K to 2 K. When the temperature was increased, we observed a decrease in the current at which the *PCR* vs I_B curve showed an inflection point (which we defined as the cutoff current, I_{co} [17]).Figure 4 b shows *PCR* vs I_B curves at several

wavelengths (1200 - 1650 nm). Consistent with the observations reported in Ref. [18], when the wavelength increased, the cutoff current increased. Figure 4 c and d show the temperature and wavelength dependence of I_{co} that we extracted from Figure 4 a and b with the procedure reported in the Supplementary Information of Ref. [17]. Based on Ref. [19], the cutoff current was expected to scale in the same way as the current at which the detector transitioned from the two-photon detection regime to the single-photon detection regime. Therefore, we used I_{co} to quantify how the bias ranges of the two-photon detection regime changed with bath temperature and excitation wavelength.

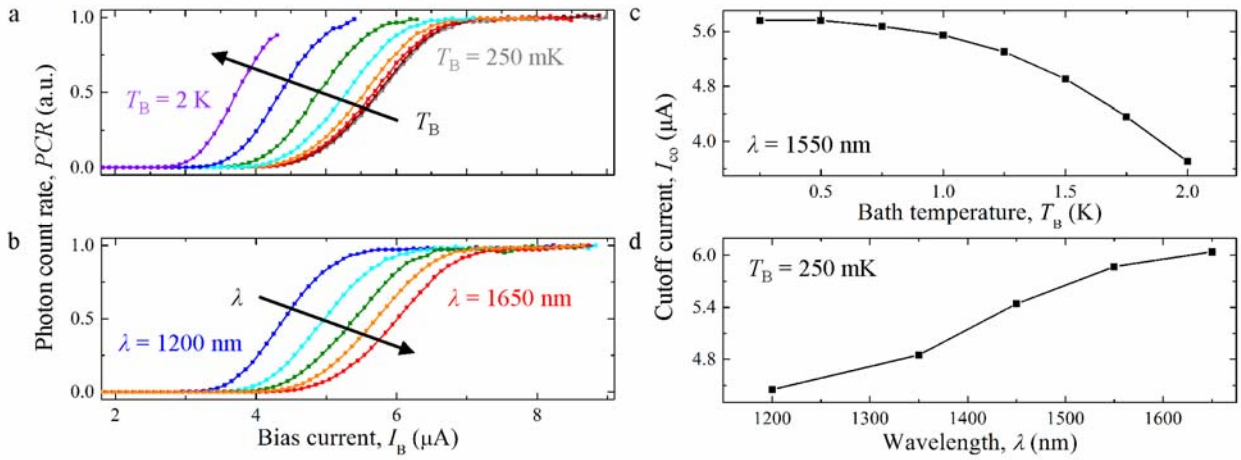

Figure 4. a. Normalized *PCR* vs I_B at bath temperatures $T = 0.25$ (gray), 0.5 (dark red), 0.75 (red), 1 (orange), 1.25 (green), 1.5 (cyan), 1.75 (blue), 2 K (violet). The excitation wavelength was $\lambda = 1550$ nm. The black arrow indicates the direction of increasing T_B. The *PCR* vs I_B curves at the different bath temperatures were normalized by the maximum *PCR* at $T = 0.25$ K. **b.** Normalized *PCR* vs I_B at wavelengths $\lambda = 1200$ nm (blue), 1350 nm (cyan), 1450 nm (green), 1550 nm (orange), 1650 nm (red). The bath temperature was $T_B = 0.25$ K. The *PCR* vs I_B curves at each wavelength were normalized by the maximum *PCR* at that wavelength. The black arrow indicates the direction of increasing λ. **c.** I_{co} vs T_B curve extracted from panel a. **d.** I_{co} vs λ curve extracted from panel b.

III. HOTSPOT RELAXATION MEASUREMENTS

To measure the hotspot relaxation time, we biased the SNSPD in the two-photon detection regime and excited it with a pair of optical pulses from the supercontinuum source separated by a variable time delay (t_D), as shown in Figure 5. We produced the optical pulse pair by coupling the laser to a Mach-Zehnder interferometer with a

variable delay in one of the arms [11]. We measured P_{click} as a function of t_D at a series of bias currents, bath temperatures, and excitation wavelengths.

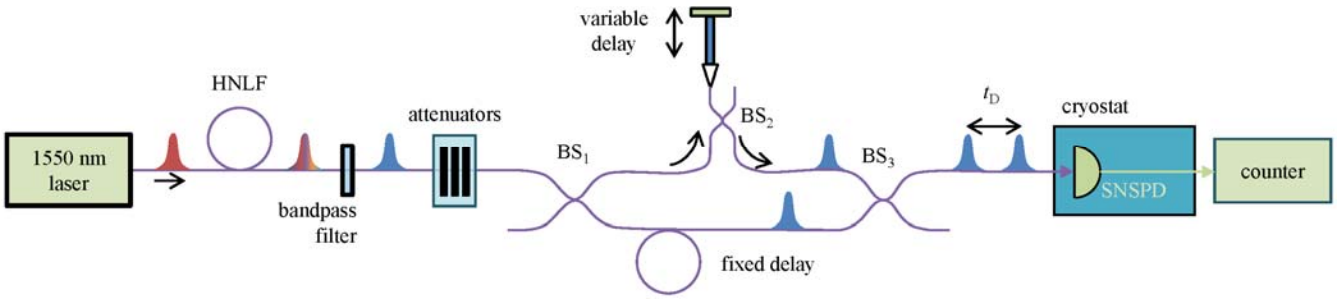

Figure 5. Experimental apparatus for the hotspot relaxation time measurements. We used a highly nonlinear fiber (HNLF) to generate a supercontinuum spanning wavelengths from 1200 – 1650 nm. The supercontinuum was filtered with band-pass filters with ~ 12 nm bandwidth. Three fiber beamsplitters (BS) and a variable delay form the Mach-Zehnder interferometer, which outputs two pulses separated by a variable time delay (t_D).

A. Bias Dependence of the Hotspot Relaxation Time

Figure 6 a shows P_{click} vs t_D curves measured at several bias currents. The P_{click} vs t_D curves had a Lorentzian shape except in the range -5 ps $\leq t_D \leq$ 5 ps, where the P_{click} exhibited oscillations due to the optical interference of overlapping pulse pairs; the data in this region are enclosed by a dashed square in Figure 6 a. Based on the measurements reported in Ref. [12], we did not expect the shape of the P_{click} vs t_D curves to depend on the bias current. However, surprisingly the P_{click} vs t_D curves measured with our device became broader as the bias current increased. No significant bias dependence was observed in Ref. [12], probably because the detector in Ref. [12] did not operate in the two-photon detection regime in the current range considered, but rather in a mixed regime between single and two-photon detection regimes.

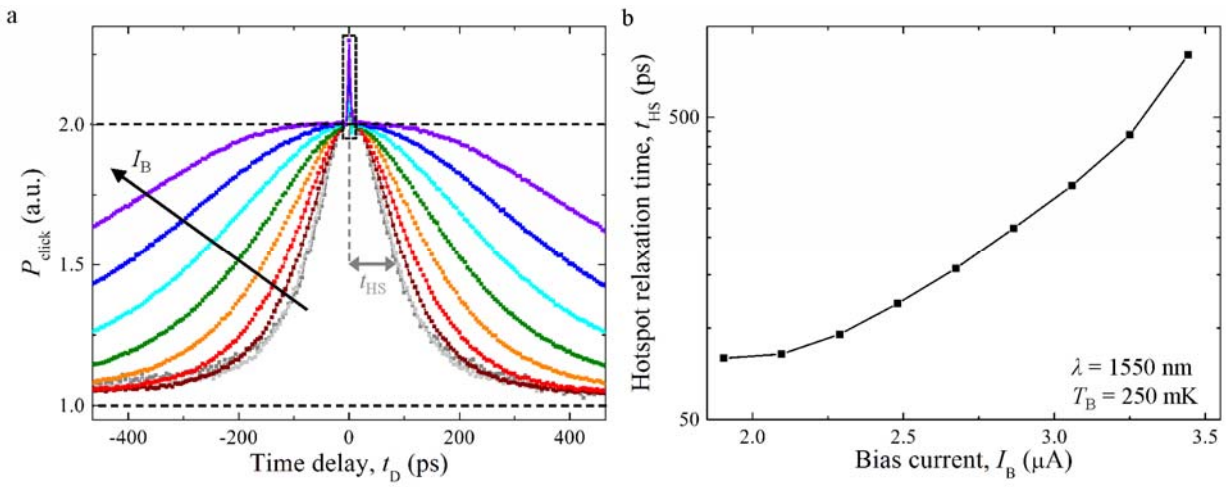

Figure 6. a. Normalized P_{click} vs t_D curves measured with the detector operating in the two-photon detection regime at I_B = 1.9 μA (dark gray); 2.1 μA (light gray, overlapped to dark gray); 2.3 μA (dark red); 2.5 μA (red); 2.7 μA (orange); 2.9 μA (green); 3.1 μA (cyan); 3.3 μA (blue); 3.5 μA (violet). t_D was varied in steps of 5 ps. The black arrow indicates the direction of increasing I_B. The dark gray arrow indicates the half width at half maximum (HWHM) of the P_{click} vs t_D curve measured at I_B = 1.9 μA. The supercontinuum source was attenuated so that P_{click} < 10 % in each individual pulse. **b.** t_{HS} vs I_B curve extracted from fits to the data in panel a. The standard deviation of all the fitted t_{HS} values was less than 1 %. These measurements were performed at λ = 1550 nm, and T_B = 0.25 K. The switching current of the device, which is defined as the maximum current the device can be biased at without switching to the normal, non-superconducting state, was I_{SW} = 8.8 μA. Note that the ordinate axis is in logarithmic scale.

We fit the experimental P_{click} vs t_D curves with Lorentzians, ignoring data in the range of the optical interference, and normalized each of the curves so that the maximum value of the corresponding Lorentzian fit curve was 2. As a result, the normalized P_{click} decayed from a value of ~ 2 to a value of ~ 1 when the time delay was increased. The shape of the P_{click} vs t_D curves can be correlated with the hotspot relaxation dynamics using an intuitive argument. Since the SNSPD operated in the two-photon detection regime, if an optical pulse created only one hotspot, the detector did not click and the hotspot cooled after some characteristic time. If the optical pulses were separated by time delays larger than the hotspot relaxation time, the detector fired only if a single optical pulse created two overlapping hotspots in the nanowires (see Figure 1 b). However, for time delays shorter than the hotspot relaxation time, two overlapping hotspots could also be created by two subsequent pulses, leading to

an increase in P_{click}. To be consistent with prior work in the literature [11, 12], we defined the hotspot relaxation time (t_{HS}) as the time delay at which this increase in P_{click} has decayed to half of its peak value.

The shape of the P_{click} vs t_D curves can be explained more quantitatively in the case of the detector operating in the two-photon detection regime with $\eta_2 \cdot \mu^2 << 1$, so Equation (1) can be approximated by $P_{click}(\mu) \sim \eta_2 \cdot \mu^2 / 2$ (see Section II.A). If the time delay between pulses is longer than the hotspot relaxation time ($t_D \gg t_{HS}$), then P_{click} is approximately equal to the sum of the probabilities from each pulse acting independently: $P_{\text{click}}\,(t_D \gg t_{HS}) \approx \eta_2\mu^2$. At short delays, where $t_D << t_{HS}$ but the two optical pulses do not overlap temporally, these pulses act as a single pulse with twice the mean photon number, doubling the click probability: $P_{\text{click}}\,(t_D \ll t_{HS}) \approx \eta_2(2\mu)^2/2 = 2\eta_2\mu^2$. As a result, we expect $P_{\text{click}}\,(t_D \ll t_{HS})/P_{\text{click}}\,(t_D \gg t_{HS}) \approx 2$, which is in agreement with the data shown in Figure 6 a.

We quantified t_{HS} as the half width at half maximum (HWHM) of the fitting curves. Figure 6 b shows the t_{HS} vs I_B curve extracted from the data shown in Figure 6 a. When I_B was increased from I_B = 1.9 μA to I_B = 3.5 μA, t_{HS} increased by one order of magnitude from t_{HS} ~ 80 ps to t_{HS} ~ 800 ps.

B. Temperature and Wavelength Dependence of the Hotspot Relaxation Time

To gain insight into the mechanism that caused t_{HS} to increase when I_B was increased, we investigated how the bias dependence of t_{HS} changed when changing T_B and λ. As shown in Figure 7 a, t_{HS} increased when T_B was increased at a fixed wavelength (squares). As shown in Figure 7 b, t_{HS} decreased when λ was increased at a fixed temperature (squares). The shape of the t_{HS} vs I_B curves measured at different temperatures and wavelengths shows a correlation with the temperature- and wavelength-dependence of the cutoff current shown in Figure 4 c and d. As shown in Figure 7 c, while the t_{HS} vs I_B curves measured at different temperatures and wavelengths differ significantly, the t_{HS} vs I_B / I_{co} curves (squares) closely follow the same trend, indicating a correlation between hotspot dynamics and single-photon sensitivity.

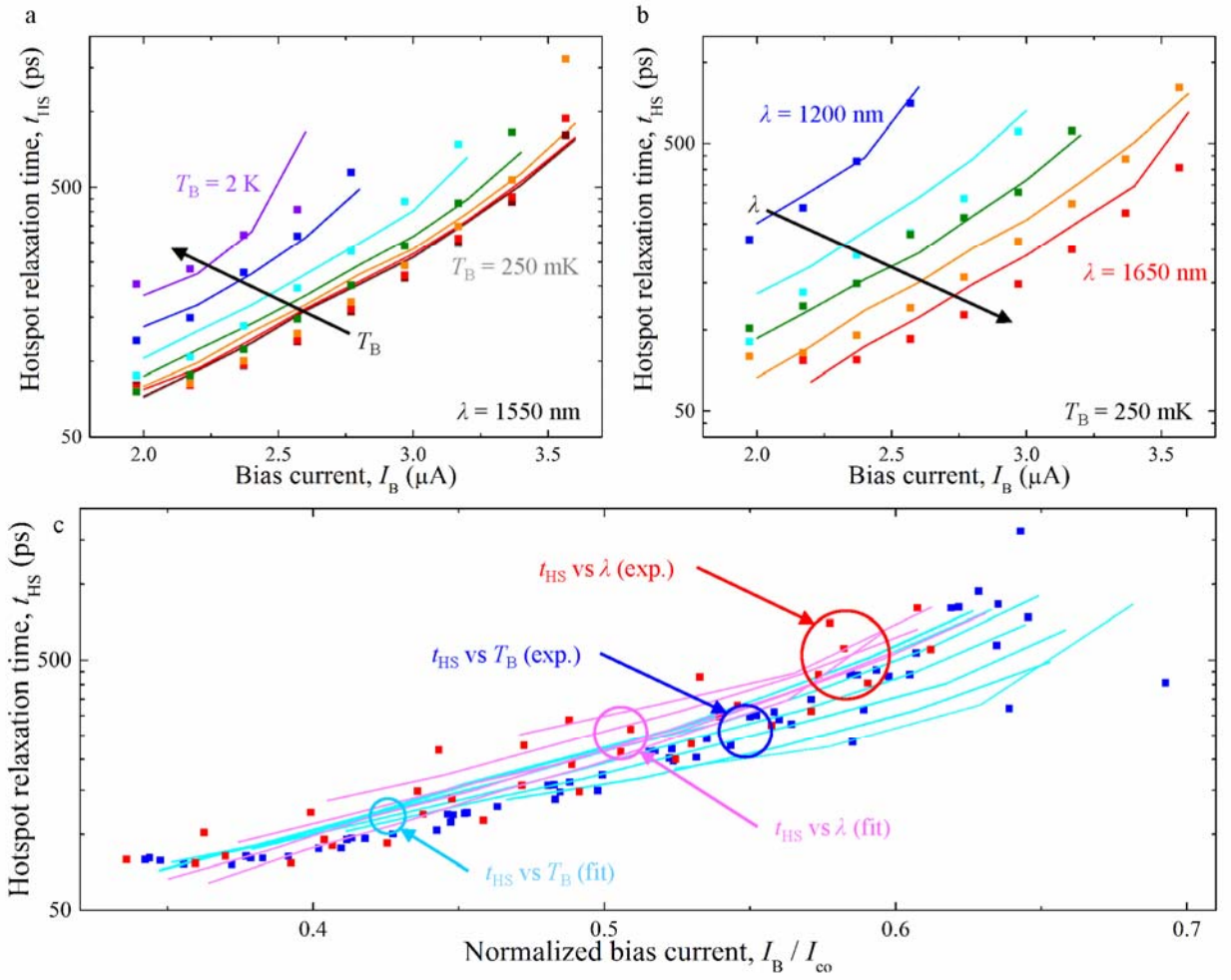

Figure 7. a. Experimental t_{HS} vs I_B curves measured at different bath temperatures (squares) and fitting curves (lines). The bath temperatures were T_B = 0.25 (gray), 0.5 (dark red, overlapping with gray), 0.75 (red), 1 (orange), 1.25 (green), 1.5 (cyan), 1.75 (blue), 2 K (violet). The excitation wavelength was λ = 1550 nm. The black arrow indicates the direction of increasing T_B. **b.** Experimental t_{HS} vs I_B curves measured at different wavelengths (squares) and fitting curves (lines). The excitation wavelengths were λ = 1200 nm (blue); 1350 nm (cyan); 1450 nm (green); 1550 nm (orange); 1650 nm (red). The bath temperature was T_B = 250 mK. The black arrow indicates the direction of increasing λ. **c.** Blue squares (cyan lines): experimental (simulated) t_{HS} vs normalized bias current measured at different temperatures (T_B = 0.25 – 2 K) and fixed wavelength (λ = 1550 nm), as shown in panel a. Red squares (magenta lines): experimental (simulated) t_{HS} vs normalized bias current measured at different wavelengths (λ = 1200 -1650 nm) and fixed bath temperature (T_B = 250 mK), as shown in panel b. The bias current of the curves measured at each temperature and wavelength were normalized by the corresponding cutoff currents from Figure 4. Note that the ordinate axis of all the graphs is in logarithmic scale.

IV. DISCUSSION

A. Theoretical Model

We have developed a theoretical model for the bias dependence of t_{HS} in which QP recombination is the dominant hotspot relaxation mechanism and QP diffusion is ignored. Since neglecting QP diffusion is in contrast with the traditional theory of hotspot dynamics [1, 20-22], our model provides insight into the physics of non-equilibrium superconductivity in disordered films. Our model solves the kinetic equation for a current-carrying superconductor, assuming a dirty superconductor model and including strong disorder-enhanced electron-electron scattering. Here, we give a brief outline of the model and its predictions. The full description of our approach is given in a separate theory paper[19], which includes details of: (1) the method for calculating the relaxation of a non-equilibrium state in a current-carrying superconductor with changing temperature, order parameter and spectrum of elementary excitations, and (2) the procedure we used to fit the experimental data. Our model quantitatively reproduces the experimentally observed decrease in t_{HS} when decreasing the bias current, decreasing the bath temperature, and increasing the excitation wavelength. Furthermore, our model provides an estimate for the t_{HS} of NbN close the experimental values[11, 12, 23] (see section IV.C).

A few picoseconds after the absorption of a photon, a non-equilibrium distribution of QPs is created through electron-phonon and electron-electron scattering [1]. Our model neglects this initial evolution of the distributions of QPs and phonons because it is expected to occur on much shorter time scales than the experimental values of t_{HS}. We thus assumed that the absorption of a photon (at time zero) instantly produces a hotspot in which the QP temperature (T_{QP}) is higher than the bath temperature (T_B). We modeled the hotspot as extending across the entire width and thickness of the nanowires, as shown in Figure 1. This picture of the hotspot is consistent with the conclusions of Ref. [24]. We also assumed that the hotspot maintains a fixed length ($l_{HS} \sim 100$ nm, see Appendix A) throughout the relaxation process. Although QP diffusion may play a significant role in establishing the hotspot size shortly after photon absorption [20-22], the experimental values of t_{HS} are consistent with the assumption that QP diffusion does not play a major role in thermalizing the QP system during further cooling of the hotspot.

Neglecting QP diffusion is against expectations based on a linear diffusion model (which assumes that the thermal conductivity of the QPs is independent of temperature) and the experimentally measured value of the diffusion coefficient of WSi in the normal state ($D = 0.75$ cm^2 / s, see Appendix B). However, two factors are likely to play a significant role in limiting the effect of QP diffusion during thermalization: (1) QP diffusion can be described more accurately by a non-linear model, which assumes that the thermal conductivity of the QPs depends on temperature in the hotspot and predicts substantially slower diffusion than the linear model; and (2) strong disorder in the nanowire results in large local fluctuations of the order parameter [25], which may enhance Andreev reflections in the thermalized distribution of QPs and restrict the expansion of the hotspot.

We have used our model to simulate the time evolution of the QP temperature (T_{QP}) after the absorption of two subsequent photons under a variety of conditions (changing t_D, I_B, and T_B). As shown in Figure 8 a, after absorption of the first photon, T_{QP} instantly increases from T_B to the excitation temperature (T_{ex}) and then starts relaxing back toward T_B. When the second photon is absorbed (after a delay time t_{D1}), T_{QP} exceeds the critical temperature (T_C) at this bias current, and the hotspot switches to the normal state, resulting in an output pulse. Figure 8 b shows the time evolution of T_{QP} for the same conditions as in Figure 8 a, except for a longer delay time ($t_{D2} > t_{D1}$). In this case, absorption of the second photon does not cause T_{QP} to exceed T_C and no click is produced. We defined a cutoff temperature (T_{co}) as the lowest QP temperature at which absorption of the second photon causes a click ($T_{QP} = T_C$). We defined the theoretical hotspot relaxation time (t_{HS}^t) as the time required for T_{QP} to reach T_{co}.

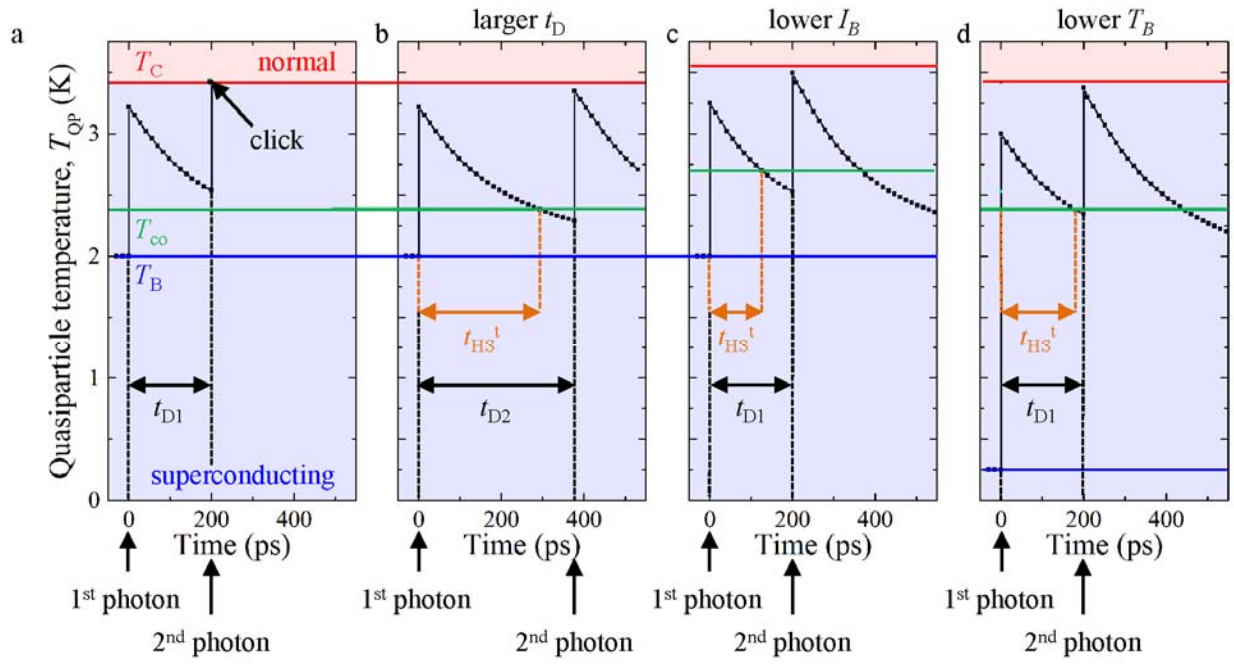

Figure 8. a. Simulated time evolution of T_{QP} (black squares) after absorption of two subsequent photons at 0 s and t_{D1} = 200 ps. The parameters of the simulation are: T_B = 2 K, T_C = 3.4 K, I_B = 2.4 μA, λ = 1500 nm. The blue line represents the bath temperature, T_B, the red line represents the critical temperature, T_C, and the green line represents a cutoff temperature of T_{co} = 2.4 K. The range of temperatures for which the hotspot is superconducting is colored in blue; the range for which the hotspot is normal (resistive) is colored in red. The critical temperature of the nanowire at zero bias is 4.5 K. **b.** Simulated time evolution of T_{QP} for the same parameters as panel a, except for a longer delay time t_{D2} = 375 ps. The theoretical hotspot relaxation time is t_{HS}^t = 310 ps. **c.** Simulated time evolution of T_{QP} for the same parameters as panel a, except for a lower bias current I_B = 2 μA. The theoretical hotspot relaxation time decreases to t_{HS}^t = 125 ps. **d.** Simulated time evolution of T_{QP} for the same parameters as panel a, except for a lower bath temperature T_B = 0.25 K. The theoretical hotspot relaxation time decreases to t_{HS}^t = 110 ps. The orange arrows highlight the theoretical hotspot relaxation time (t_{HS}^t).

Our model neglects any inhomogeneities in the device properties and fluctuations in the detection and relaxation processes. Our model also assumes that even minimal spatial overlap between two hotspots (see Figure 1 b) can produce a click if $t_D \leq t_{HS}^t$ and no click if $t_D > t_{HS}^t$. Therefore, the P_{click} vs t_D curves predicted by the model have sharp rectangular profiles, in contrast to the Lorentzian profiles observed in the experimental data shown in **Figure 6** a. A similarly idealized model of single-photon detection [20] predicts *PCR* vs I_B curves with step-like shapes, in contrast to the sigmoidal shapes observed experimentally, as shown in `Figure 4` a and b. We expect

that more sophisticated models that account for inhomogeneities and fluctuations will better match experimental results.

B. Comparison to WSi Data

The theoretical model we developed provides an interpretation of the experimental results shown in Figure 6 and 7. Based on our model, we can attribute the bias-dependence of hotspot relaxation shown in Figure 6 to the increase of T_{co} when I_B is decreased. As shown Figure 4 a, the switching current of the detector increased when T_B was decreased, which implies that the critical temperature of the nanowire increased when I_B was decreased (see also Figure 3 a in Ref. [19]). As shown in Figure 8 c, at lower bias current the critical temperature increased, leading to a significant increase in T_{co}. The excitation temperature and the relaxation transient of T_{QP} are not significantly affected by the change in bias current. Therefore, if I_B is decreased, T_{QP} relaxes from T_{ex} to T_{co} in a shorter time, in agreement with the results in Figure 6.

The dependence of t_{HS} on T_B shown in Figure 7 a can be attributed to the temperature dependence of the relaxation rate of T_{QP}. As shown in Figure 8 d, although T_B does not affect T_{co}, T_B affects T_{ex} and the relaxation transient of T_{QP}. Our model predicts that: (1) at lower bath temperature, T_{ex} is lower, and (2) the relaxation rate of T_{QP} is higher when T_{QP} is further away from T_B (the electron relaxation rate in normal metals shows similar behavior [26]). Consequently, $t_{HS}{}^t$ decreases when the bath temperature is decreased, in agreement with the experimental results in Figure 7 a.

We can attribute the dependence on λ shown in Figure 7b to the dependence of the excitation and cutoff temperatures on the photon energy. According to our model, with longer-wavelength photons: (1) the increase of T_{QP} after absorption of a photon ($T_{ex} - T_B$) is smaller; and (2) T_{co} is higher because the temperature difference $T_C - T_{co}$ is proportional to the photon energy. At longer excitation wavelengths, T_{ex} is lower and T_{co} is higher, so T_{QP} decreases from T_{ex} to T_{co} more quickly, in agreement with the experimental results shown in Figure 7 b.

The solid curves in Figure 7 show fits to the experimental data (squares) calculated with our model. We fit all the experimental data in Figure 7 a using four fitting parameters: (1) the phonon bottleneck parameter $\gamma = \tau_{esc} / \tau_{ph\text{-}e}$, where τ_{esc} is the phonon escape time to the substrate and $\tau_{ph\text{-}e}$ is the phonon-electron scattering time; (2) the characteristic quasiparticle time of WSi, τ_0 (as defined in Ref. [27]); (3) the energy deposition factor $\delta = \chi / \varepsilon_c$,

where $\chi = E_{ex} / E_{\lambda}$ is the photon yield, which we defined as the ratio of the energy deposited in the hotspot after the absorption of the photon (E_{ex}) to the photon energy (E_{λ}), and ε_c is the energy of the condensate in the hotspot volume; and (4) a temperature offset (ΔT_B), which we defined as the difference between the simulated and experimental bath temperatures. The values of the fitting parameters are: $\gamma = 0.3$, $\tau_0 = 994$ ps, $\delta = 325$ meV^{-1} and $\Delta T_B = 0.5$ K. The fitting value of γ indicates that non-equilibrium phonons could be re-absorbed by the condensate and the QPs before escaping into the substrate, slowing down the recombination. The fitting value of τ_0 is commensurate to the characteristic quasiparticle time of materials with order parameter similar to WSi [27]. The fitting value of δ indicates that only a small fraction ($\chi = 0.26$) of the photon energy was deposited into the electronic system, which is likely due to: (1) the energy partition between QPs and non-pair-breaking phonons, and (2) the loss of athermal phonons [28]. The temperature offset of 0.5 K indicates that the detector may not have been at the base temperature of the refrigerator, possibly due to the laser heating the detector. The fits deviated from the experimental data at larger bias currents because at high bias currents the cut-off temperature T_{co} was only marginally higher than T_B and the description of non-equilibrium phonon distribution developed in our model [19] may not have been accurate in those conditions.

We fit all of the experimental data in Figure 7 b using only three fit parameters: $\gamma = 0.3$, $\tau_0 = 878$ ps and $\delta = 325$ meV^{-1}. These values are consistent with those used to fit the data in Figure 7 a.

Our model can also accurately predict the temperature- and wavelength-dependence of I_{co}. Using the values of the fitting parameters obtained from the fits shown in Figure 7 a and b, we could reproduce the shape of the experimental I_{co} vs T_B and I_{co} vs λ curves in Figure 4 c and d (see Figure 11 in Ref. [19]). Figure 7 c shows the experimental and simulated t_{HS} vs I_B / I_{co} curves at different temperatures and wavelengths. The four families of curves closely follow the same trend. Since I_{co} is expected to scale in the same way as the current at which the SNSPD switches from the two-photon to the single-photon detection regime [19], the trend shown in Figure 7 c suggests that the increase in hotspot relaxation time when the bias current approaches I_{co} correlates to an increase in the single-photon sensitivity of the nanowires. The correlation between the hotspot dynamics and SNSPD sensitivity is discussed in detail in Ref. [19].

C. Comparison to NbN Data

We also used our model to reproduce the data reported in Ref. [11, 12] for NbN nanowires. We obtained $t_{HS}^{t} = 20$ ps for $I_B / I_{SW} = 0.5$, in agreement with the experimental values [11, 12], by assuming: (1) NbN on sapphire as in Ref. [12], because of the known material parameters; (2) excitation wavelength $\lambda = 1064$ nm as in Ref. [12]; (3) $\gamma = 0.6$ (following Ref. [23], which reports on NbN films of similar thickness on sapphire substrates); (4) $\delta = 130$ meV^{-1}; and (5) $\tau_0 = 104$ ps. Since the energy gap of NbN is a factor of ~ 2.5 larger than that of WSi, assuming $\delta = 130$ meV^{-1} and the same hotspot volume in WSi and NbN nanowires, we estimated $\chi_{NbN} / \chi_{WSi} \sim 1.9$. The larger photon yield of NbN with respect to WSi is consistent with the higher phonon bottleneck parameter of NbN ($\gamma_{NbN} = 0.6$ [23], $\gamma_{WSi} = 0.3$), resulting in lower loss of athermal phonons. The assumption that $\tau_0 \sim 100$ ps is based on the scaling of the characteristic quasiparticle time with the critical temperature [27]: $\tau_0^{-1} \sim T_C^3$. Provided that the electron-phonon constants in NbN and WSi are close, for NbN: $\tau_{0,NbN} \approx (T_{C,WSi} / T_{C,NbN})^3 \cdot \tau_{0,WSi} \approx 0.1 \cdot \tau_{0,WSi}$. Table 1 summarizes the parameters of our model and the values we used to fit the data in Figure 7 a and b and in Ref. [11, 12].

Table 1. Summary of the parameters for the hotspot relaxation model [29].

Symbol	Description	Value WSi (Figure 5 a)	Value WSi (Figure 5 b)	Value NbN (Ref. [11, 12])
γ	phonon bottleneck parameter	0.3	0.3	0.6
τ_0	characteristic quasiparticle time	994 ps	878 ps	104 ps
δ	energy deposition factor	325 meV^{-1}	325 meV^{-1}	130 meV^{-1}
ΔT_B	temperature offset	0.5 K	NA	NA

Hotspot relaxation in current-carrying NbN nanowires has been measured at a single [11] or a few bias currents (0.48 to 0.55I_{SW}) [12], probably because the detectors used in Ref. [11, 12] operated in the two-photon detection regime for only a narrow bias range. By contrast, our WSi SNSPD operated in the two photon regime over a large bias range (0.2 to 0.4I_{SW}), which allowed us to study the bias dependence of t_{HS}. Our estimate of t_{HS} in NbN indicates

that our model may be of use in simulating NbN devices, but a full detailed comparison of hotspot dynamics in NbN and WSi will have to await further bias-dependent experimental data.

D. Normal Metal Limit

To offer further insight into the QP relaxation process described by our model [19], we may draw a parallel with the thermalization of a non-equilibrium distribution of electrons in a normal metal. Such a comparison is a great oversimplification that misses many important details. Nonetheless, it allows a qualitative understanding of the origin of some of the effects we observed experimentally (see section III).

In the normal metal limit, we neglected diffusion, coherence factors in collision integrals, and the time derivative of the order parameter. In this limit, the expression for energy relaxation derived in Ref. [26] can be written as:

$$C\frac{\partial T}{\partial t} = -K\left(T^5 - T_{\mathrm{B}}^5\right) \qquad (2)$$

where C is the electronic heat capacity and K is the thermal conductance. In the limit $T >> T_{\mathrm{b}}$, and assuming C to be proportional to T , Equation (2) can be written as:

$$\frac{\partial \bar{T}}{\partial \bar{t}} = \bar{T}^4 \qquad (3)$$

Equation (3) can be interpreted as a simplified form of Equation (21) in Ref. **[19]**. The top bars in this expression denote that temperature is in units of T_{c} and time is in units of the characteristic electron-phonon relaxation time. The solution of Equation (3) is $\bar{T}(t) = \bar{T}_{ex}\left(\bar{T}_{ex}{}^3\bar{t} + 1\right)^{-1/3}$, and the predicted hotspot relaxation time is:

$$\bar{t}_{\mathrm{HS}}^{\mathrm{t}} = \left(\bar{T}_{\mathrm{co}}{}^{-3}(I_B, \lambda) - \bar{T}_{\mathrm{ex}}{}^{-3}(I_{\mathrm{B}}, T_{\mathrm{B}})\right) \qquad (4)$$

The dependence of $\bar{t}_{\mathrm{HS}}^{\mathrm{t}}$ on $\bar{T}_{co}(I_B, \lambda)$ in Equation (4) is consistent with the significant decrease of $t_{\mathrm{HS}}^{\mathrm{t}}$ with decreasing bias current shown in Figure 6 and Figure 8 c. The dependence of $\bar{t}_{\mathrm{HS}}^{\mathrm{t}}$ on T_{B} through $\bar{T}_{\mathrm{ex}}$ is consistent with the decrease of $t_{\mathrm{HS}}^{\mathrm{t}}$ with decreasing bath temperature shown in Figure 7 a and Figure 8 d.

V. SUMMARY

We observed that the hotspot relaxation time of a superconducting nanowire can be increased by increasing the bias current, the temperature or the photon energy. We developed a model that explains and quantitatively reproduces all of the experimental data. The effect we discovered provides insight into non-equilibrium superconductivity and has important implications for superconducting detectors. For example, our results suggest that the quasiparticle relaxation time of MKIDs based on disordered materials [3, 31] may be increased by DC-biasing the MKID inductor, which would increase the MKID sensitivity. Furthermore, the shortest hotspot relaxation time measured in our WSi SNSPD is a factor of ~ 4 longer than that measured with NbN (15-30 ps [1, 11, 12, 23]), indicating a significant difference in material properties that was not well understood and not previously predicted. The longer t_{HS} of WSi may limit the maximum count rate of WSi SNSPDs to a lower value than NbN SNSPDs, due to latching [32, 33] or afterpulsing [34].

ACKNOWLEDGMENTS

Part of the research was carried out at the Jet Propulsion Laboratory, California Institute of Technology, under a contract with the National Aeronautics and Space Administration. AK and CL gratefully acknowledge financial support from the Engineering and Physical Sciences Research Council.

APPENDIX A: HOTSPOT SIZE ESTIMATE

The single-photon system detection efficiency can be decomposed as:

$$\eta_1 = \eta_{\text{couple}}\eta_{\text{absorb}}\eta_{\text{QE1}} \quad (5)$$

where η_{couple} is the coupling efficiency, η_{absorb} is the absorption efficiency and η_{QE1} is the single-photon internal quantum efficiency. η_{couple} is the probability that a photon in the guided mode of the fiber impinges on the active area of the detector. η_{absorb} is the probability that a photon incident on the active area is absorbed in the detector. η_{QE1} is the probability that one photon absorbed in the detector triggers a response pulse.

Similarly, the two-photon efficiency can be decomposed as:

$$\eta_2 = \eta_{\text{couple}}^2 \eta_{\text{absorb}}^2 \eta_{\text{overlap}} \eta_{\text{QE2}} \quad (6)$$

If two photons are in the fiber, the product $\eta_{\text{couple}}^2 \eta_{\text{absorb}}^2$ represents the probability that both photons are coupled to and absorbed in the active area of the detector, creating two hotspots. η_{overlap} is the probability that these two hotspots overlap each other, and η_{QE2} is the probability that these two overlapping hotspots lead to an output voltage pulse.

We assumed that: (1) at sufficiently high bias currents, the single- and two-photon detection efficiencies plateau to values that we label η_1^{plateau} and η_2^{plateau}; (2) $\eta_1^{\text{plateau}} \approx \eta_2^{\text{plateau}} \approx 1$ (at present, the most precise lower bound for of η_1^{plateau} is ~ 93% [16]); and (3) the hotspot size is independent of bias current. Based on our assumptions, the overlap probability can be estimated as:

$$\eta_{\text{overlap}} \approx \frac{\eta_2^{\text{plateau}}}{\left(\eta_1^{\text{plateau}}\right)^2}. \quad (7)$$

This probability can be related to the size of each hotspot relative to the active area of the detector. Treating the detector as a series of independent wires, we calculated the probability that any two hotspots overlap, under the assumption that each hotspot is rectangular, with a width of 130 nm (the nanowire width) and length l_{HS}. From a series of measurements similar to those in Figure 3, we estimated that $\eta_{\text{overlap}} \approx 5.4 \times 10^{-4}$ and $l_{\text{HS}} \approx 100$ nm for an excitation wavelength $\lambda = 1550$ nm.

APPENDIX B: DIFFUSIVITY OF WSi

The temperature dependence of the upper critical magnetic field (B_{C2}) provides information on material properties of thin films. The electron diffusion coefficient (D) is obtained from the slope of the B_{C2} vs T_B curve. In the limit of a dirty superconductor, the electron diffusivity D can be expressed as follows [35]:

$$D\left[\text{cm}^2\text{sec}^{-1}\right] = \frac{1.097}{\left[-\frac{dB_{C2}(T_B)}{dT}\right]_{T_B=T_c}\left[\text{TK}^{-1}\right]} \quad (8)$$

We measured the temperature dependence of the upper critical magnetic field of two WSi films of different thickness $d = 4.5$ and 9 nm. We measured the resistance (R) of the films as a function of the magnetic field (B)

applied perpendicular to the surface of the films at different temperatures. Figure 9 a shows the R vs B curves measured at different temperatures. We defined B_{C2} as the field at which the resistance of the films became half of the normal state value. Figure 9 b shows the B_{C2} vs T_B curves for the 9 nm and 4.5 nm-thick films.

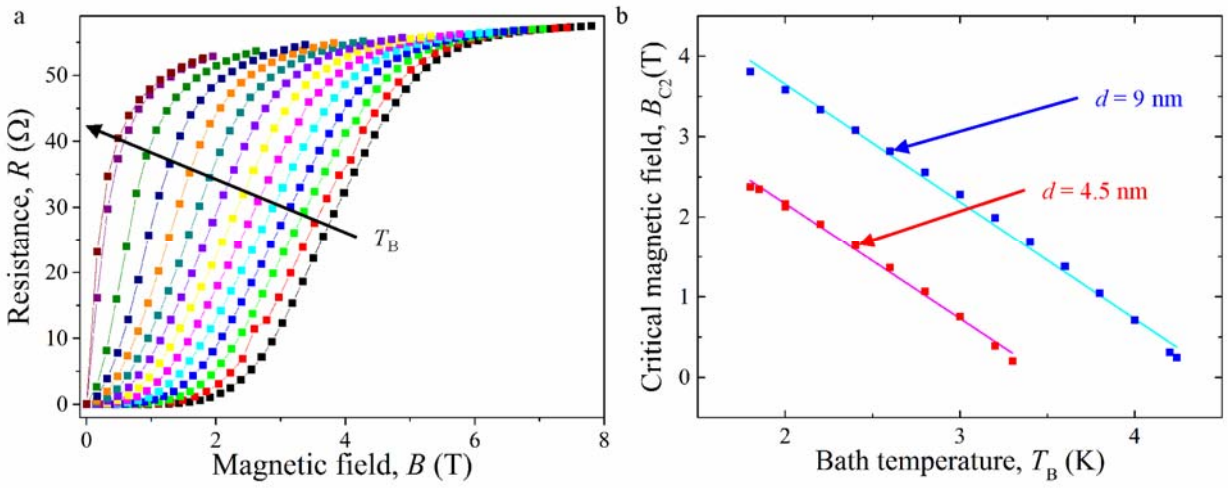

Figure 9. a. R vs B curves for 9 nm WSi films at different temperatures T_B = 4.5 K to 1.8 K. The black arrow indicates the direction of increasing T_B. **b.** Squares: measured temperature dependence of the critical magnetic field for d = 4.5 nm (red) and 9 nm (blue). Solid lines: linear fits to the data. The slopes are - 1.44 T / K and - 1.46 T / K for the 4.5 nm and 9 nm-thick films.

The calculated values for WSi electronic diffusion coefficient based on Equation (8) are 0.76 cm^2 / s and 0.75 cm^2 / s for 4.5 nm and 9 nm thick films. We assumed that the susceptibility of WSi was similar to that of tungsten (6.8 x10^{-5}). A linear extrapolation of the measured $B_{C2}(T)$ down to $T = 0$ K can be related to the Ginzburg-Landau coherence length ($\xi_{GL}(0)$), at $T = 0$ K from the following equation [35]:

$$B_{C2}(T) = \frac{\Phi_0}{2\pi\xi(T)^2} \qquad (9)$$

where $\Phi_0 = h / 2e$ is the magnetic-flux quantum and e is the electron charge. Using Equation (9), we extracted coherence length values of 8.09 nm and 7.08 nm for the 4.5 nm and 9 nm-thick WSi films. However, in the limit of a dirty superconductor, a linear extrapolation of the measured $B_{C2}(T)$ down to $T = 0$ K, overestimates the real upper critical field at zero temperature [35] and consequently underestimates the superconducting coherence length. A more realistic value of $B_{C2}(0)$ is given by [36]:

$$B_{C2}(0) = 0.69 T_c \left[\frac{dB_{C2}(T)}{dT}\right]_{T=T_c} \qquad (10)$$

Using this value of $B_{C2}(0)$ in equation (10) we calculated a coherence length of 9.72 nm and 8.51 nm for the 4.5 nm and 9 nm-thick WSi films.

REFERENCES

[1] A. D. Semenov, G. N. Gol'tsman, and R. Sobolewski, Supercond. Sci. Technol. **15**, R1 (2002).

[2] P. K. Day, H. G. LeDuc, B. A. Mazin, A. Vayonakis, and J. Zmuidzinas, Nature **425**, 817 (2003).

[3] J. Gao, M. R. Vissers, M. O. Sandberg, F. C. S. d. Silva, S. W. Nam, D. P. Pappas, D. S. Wisbey, E. C. Langman, S. R. Meeker, B. A. Mazin, H. G. Leduc, J. Zmuidzinas, and K. D. Irwin, Appl. Phys. Lett. **101**, 142602 (2012).

[4] A. Peacock, P. Verhoeve, N. Rando, A. van Dordrecht, B. G. Taylor, C. Erd, M. A. C. Perryman, R. Venn, J. Howlett, D. J. Goldie, J. Lumley, and M. Wallis, Nature **381**, 135 (1996).

[5] G. N. Gol'tsman, O. Okunev, G. Chulkova, A. Lipatov, A. Semenov, K. Smirnov, B. Voronov, A. Dzardanov, C. Williams, and R. Sobolewski, Appl. Phys. Lett. **79**, 705 (2001).

[6] A. Engel, J. J. Renema, K. Il'in, and A. Semenov, Supercond. Sci. Technol. **28**, 114003 (2015).

[7] A. G. Kozorezov, A. F. Volkov, J. K. Wigmore, A. Peacock, A. Poelaert, and R. den Hartog, Phys. Rev. B **61**, 11807 (2000).

[8] M. Beck, M. Klammer, S. Lang, P. Leiderer, V. V. Kabanov, G. N. Gol'tsman, and J. Demsar, Phys. Rev. Lett. **107**, 177007 (2011).

[9] R. P. S. M. Lobo, J. D. LaVeigne, D. H. Reitze, D. B. Tanner, Z. H. Barber, E. Jacques, P. Bosland, M. J. Burns, and G. L. Carr, Phys. Rev. B **72**, 024510 (2005).

[10] R. D. Averitt and A. J. Taylor, J. Phys.: Condens. Matter **14**, R1357 (2002).

[11] Z. Zhou, G. Frucci, F. Mattioli, A. Gaggero, R. Leoni, S. Jahanmirinejad, T. B. Hoang, and A. Fiore, Phys. Rev. Lett. **110**, 133605 (2013).

[12] R. W. Heeres and V. Zwiller, Appl. Phys. Lett. **101**, 112603 (2012).

[13] D. Bitauld, F. Marsili, A. Gaggero, F. Mattioli, R. Leoni, S. Jahanmirinejad, F. Lévy, and A. Fiore, Nano Lett. **10**, 2977 (2010).

[14] M. K. Akhlaghi, A. H. Majedi, and J. S. Lundeen, Opt. Express **19**, 21305 (2011).

[15] B. Baek, A. E. Lita, V. Verma, and S. W. Nam, Appl. Phys. Lett. **98**, 251105 (2011).

[16] F. Marsili, V. B. Verma, J. A. Stern, S. Harrington, A. E. Lita, T. Gerrits, I. Vayshenker, B. Baek, M. D. Shaw, R. P. Mirin, and S. W. Nam, Nature Phot. **7**, 210 (2013).

[17] F. Marsili, F. Najafi, E. Dauler, F. Bellei, X. Hu, M. Csete, R. J. Molnar, and K. K. Berggren, Nano Lett. **11**, 2048 (2011).

[18] F. Marsili, F. Bellei, F. Najafi, A. Dane, E. A. Dauler, R. J. Molnar, and K. K. Berggren, Nanolett. **12**, 4799 (2012).

[19] A. G. Kozorezov, C. Lambert, F. Marsili, M. J. Stevens, V. B. Verma, J. A. Stern, R. Horansky, S. Dyer, S. Duff, D. P. Pappas, A. Lita, M. D. Shaw, R. P. Mirin, and S. W. Nam, Physical Review B **92**, 064504 (2015).

[20] A. D. Semenov, G. N. Gol'tsman, and A. A. Korneev, Physica C **351**, 349 (2001).

[21] A. Semenov, A. Engel, H. W. Hübers, K. Il'in, and M. Siegel, Eur. Phys. J. B **47**, 495 (2005).

[22] A. Engel, J. Lonsky, X. Zhang, and A. Schilling, Applied Superconductivity, IEEE Transactions on **PP**, 1 (2014).

[23] K. S. Il'in, M. Lindgren, M. Currie, A. D. Semenov, G. N. Gol'tsman, R. Sobolewski, S. I. Cherednichenko, and E. M. Gershenzon, Appl. Phys. Lett. **76**, 2752 (2000).

[24] J. J. Renema, R. Gaudio, Q. Wang, Z. Zhou, A. Gaggero, F. Mattioli, R. Leoni, D. Sahin, M. J. A. de Dood, A. Fiore, and M. P. van Exter, Phys. Rev. Lett. **112**, 117604 (2014).

[25] B. Sacépé, C. Chapelier, T. I. Baturina, V. M. Vinokur, M. R. Baklanov, and M. Sanquer, Phys. Rev. Lett. **101**, 157006 (2008).

[26] P. B. Allen, Physical Review Letters **59**, 1460 (1987).

[27] S. B. Kaplan, C. C. Chi, D. N. Langenberg, J. J. Chang, S. Jafarey, and D. J. Scalapino, Phys. Rev. B **14**, 4854 (1976).

[28] A. G. Kozorezov, C. J. Lambert, S. R. Bandler, M. A. Balvin, S. E. Busch, P. N. Nagler, J.-P. Porst, S. J. Smith, T. R. Stevenson, and J. E. Sadleir, Phys. Rev. B **87**, 104504 (2013).

[29] 1, The fitting values of τ_0 reported in this paper differ from the values reported in Ref. [19] by a factor of two, due to a typo in Ref. [19]. Since the fitting parameter τ_0 was used to match the experimental and simulated t_{HS} vs I_B curves along the vertical axis, changing τ_0 did not change the values of the fitting parameters δ, γ and ΔT_B, which were used to match the shape of the two sets of curves. (1).

[30] F. Marsili, D. Bitauld, A. Fiore, A. Gaggero, F. Mattioli, R. Leoni, M. Benkahoul, and F. Lévy, Opt. Express **16**, 3191 (2008).

[31] P. Szypryt, B. A. Mazin, B. Bumble, H. G. Leduc, and L. Baker, IEEE Trans. Appl. Supercond. **25**, 1 (2015).

[32] J. K. W. Yang, A. J. Kerman, E. A. Dauler, V. Anant, K. M. Rosfjord, and K. K. Berggren, IEEE Trans. Appl. Supercond. **17**, 581 (2007).

[33] A. J. Kerman, J. K. W. Yang, R. J. Molnar, E. A. Dauler, and K. K. Berggren, Phys. Rev. B **79**, 100509 (2009).

[34] F. Marsili, F. Najafi, E. Dauler, R. J. Molnar, and K. K. Berggren, Appl. Phys. Lett. **100**, 112601 (2012).

[35] A. Semenov, B. Günther, U. Böttger, H. W. Hübers, H. Bartolf, A. Engel, A. Schilling, K. Ilin, M. Siegel, R. Schneider, D. Gerthsen, and N. A. Gippius, Phys. Rev. B **80**, 054510 (2009).

[36] A. Shoji, S. Kiryu, and S. Kohjiro, Appl. Phys. Lett. **60** (1992).